

Detector Development for HUBS I: Initial Testing of Small-Area TES Microcalorimeters

Naihui Chen, Jian Ma, Sifan Wang*, Qian Wang, Guanhua Gao, Qing Yu, Yajie Liang, Yaowu Song, Jingyi Zhang, Wei Cui*

Low Temperature Detector Lab, Department of Astronomy, Tsinghua University, Beijing, 100084, China

Abstract

We report progress on the ongoing development of microcalorimeter detector technology for the Hot Universe Baryon Surveyor (HUBS) mission. We show the results from testing and characterizing selected pixels in a 10×10 microcalorimeter array. The microcalorimeter is based on a Mo/Cu transition-edge sensor (TES) coupled to an Au absorber. To better understand the properties of the devices, we have first measured the energy resolution of a selected pixel in a TES array of the same design with a pulsed laser system that produces 3 eV photons, and found that individual photon peaks are easily resolved with the TES, indicating good performance. We have then exposed the microcalorimeter array to radiation from a ^{55}Fe source, and found that the pixels tested show energy resolutions as good as 3.8 ± 0.2 eV at 5.9 keV. The energy resolution is found to vary monotonically with the bias point for all the devices, showing little evidence for the presence of the so-called excess noise. This is consistent with the results from modeling the measured noise spectrum. The effects of thermal crosstalk are evident, leading to the degradation of energy resolution.

Keywords:

TES, microcalorimeter, energy resolution, thermal crosstalk, HUBS

*To whom correspondence should be addressed. Email: sifanwang@tsinghua.edu.cn, cui@tsinghua.edu.cn

1. Introduction

The Standard Cosmological Model (also known as the Λ CDM model) attributes about 5% of the energy density of the present-day universe to normal matter (also known as baryonic matter), which is the observable, and the rest to new physics (specifically dark matter and dark energy). The results from optical surveys indicate that, as the universe evolves, more and more cosmic baryons seem to go “missing”, with only about half are detected in the present-day universe, leading to the long-standing “missing baryon problem” [1]. On the theoretical front, cosmological simulations suggest that, during the formation of structures, some of the baryons may be heated to about 10^6 K and be present in a gaseous phase of very low density. Such hot baryons would radiate very weakly in the soft X-ray band, not detectable with current observing facilities and thus “missing”.

A non-dispersive, high-resolution X-ray spectrometer would make it possible to detect the “missing” baryons [2], through narrow-band imaging and X-ray spectroscopy, because the spectrum of their radiation is expected to be dominated by emission lines. To this end, the HUBS project has been proposed [3]. HUBS will be equipped with an array of microcalorimeters. A microcalorimeter consists mainly of three components [4]: an effective X-ray absorber, a sensitive temperature transducer, and a weak thermal link. The energy of an incident X-ray photon is deposited in the absorber and is thermalized, causing an increase in the temperature of the device. The temperature transducer senses the temperature change and converts the thermal signal to an electrical signal that is read out. After the thermal energy is transferred to the heat sink through the thermal link, the temperature of the device recovers, and it is ready for the arrival of the next photon.

Therefore, every X-ray photon produces a pulse signal, with its amplitude proportional to the energy of the incident photon. The accuracy in measuring the pulse amplitude, in the presence of noise, determines the energy resolution of the microcalorimeter. Often, a thermistor is chosen as the temperature transducer. In this case, the theoretical limit of energy resolution is expressed by [5]

$$\Delta E = \xi \sqrt{\frac{k_B T_0^2 C}{\alpha}}, \quad (1)$$

where k_B is the Boltzmann constant, ξ a dimensionless factor, T_0 the microcalorimeter temperature, C the heat capacity, and $\alpha = d \log R / d \log T$ the temperature sensitivity of the thermistor $R(T)$.

The challenge for developing HUBS detector lies in the difficulty of balancing the need for both large-area pixels and high energy resolution [6]. In this work, however, we present results from testing initial batches of 10×10 microcalorimeter arrays of smaller-area pixels. The temperature transducer is based on the superconducting transition-edge sensor (TES) technology [7]. The TES is made of a Mo/Cu bilayer film, and the absorber is made of pure Au and of area $240 \times 240 \mu\text{m}^2$.

2. Device Fabrication

The fabrication of the detector array basically follows the process described in [6]. The base detector material is a Mo/Cu bilayer film [8]. The bilayer film is deposited, via DC magnetron sputtering, on a Si wafer with both sides covered with low-stress SiO and SiN thin films. The thickness of the Mo or Cu layer is fine-tuned so that the superconducting transition temperature (T_c) of the bilayer is around 80 mK. The bilayer film is patterned and processed through a number of lithography and etching steps, to produce Mo/Cu TES arrays of varying designs. The edge of a TES is specially treated to significantly enhance the steepness of the superconducting transition [8]. The Au absorbers are then added to the TES array via electroplating. In this work, the size of the absorber is $240 \mu\text{m} \times 240 \mu\text{m}$, and the thickness is around $2 \mu\text{m}$. The absorber is supported by six stems, with four corner ones on SiN and two central ones on TES (see Fig. 1). We note that the devices tested here have not undergone Si back-side etching.

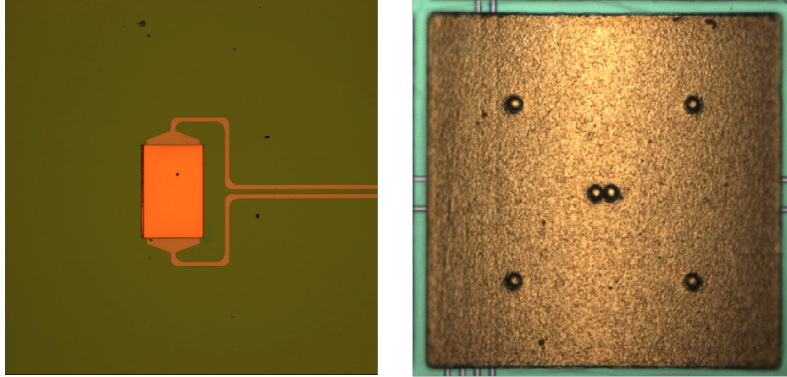


Figure 1: Left: Micrograph of the Mo/Cu TES with Mo leads. The size of the TES is $120\ \mu\text{m} \times 80\ \mu\text{m}$. Right: Micrograph of the microcalorimeter with an Au absorber, which is connected to the TES via two central stems. The size of the TES in this microcalorimeter is $60\ \mu\text{m} \times 20\ \mu\text{m}$, and the leads are made of Nb. The size of the absorber is $240\ \mu\text{m} \times 240\ \mu\text{m}$.

3. Experiment Setup

The measurements are carried out in a dilution refrigerator, with a setup that is similar to the one described in [6]. The sample box is mounted on the mixing-chamber stage and cooled below 100 mK. The device under test is read out with an input SQUID and a SQUID array, which are mounted on the cold stage, followed by a room-temperature flux-locked loop [9] for linearized signal conditioning. A voltage bias is applied through a small shunt resistor to operate the TES in a negative electrothermal-feedback mode.

4. TES Characterization

4.1. I - V Measurements

We have obtained the R - T curve of a TES pixel that is selected from a 10×10 array, and found that its normal-state resistance (R_n) is $60\ \text{m}\Omega$. By sweeping the bias voltage, we have measured its I - V characteristics, from the normal state to the superconducting state, and the results are shown in Fig. 2, for different base temperatures of the heat sink, from which a relationship between power dissipation and base temperature (P - T curve) is derived. Assuming the thermal conductance of the weak link is a power-law function of temperature,

$$G = G_0 \left(\frac{T}{T_c} \right)^{n-1}, \quad (2)$$

we have

$$P = \int_{T_b}^{T_c} GdT = \frac{G_0}{nT_c^{n-1}}(T_c^n - T_b^n), \quad (3)$$

where T_b is the base temperature, and the TES sits at T_c . Applying it to the measured P - T curve of the device, we show the best fit in Fig. 2 (right panel), with $G_0 = 221$ pW/K, $T_c = 73.5$ mK and $n = 4.0$ being the corresponding values.

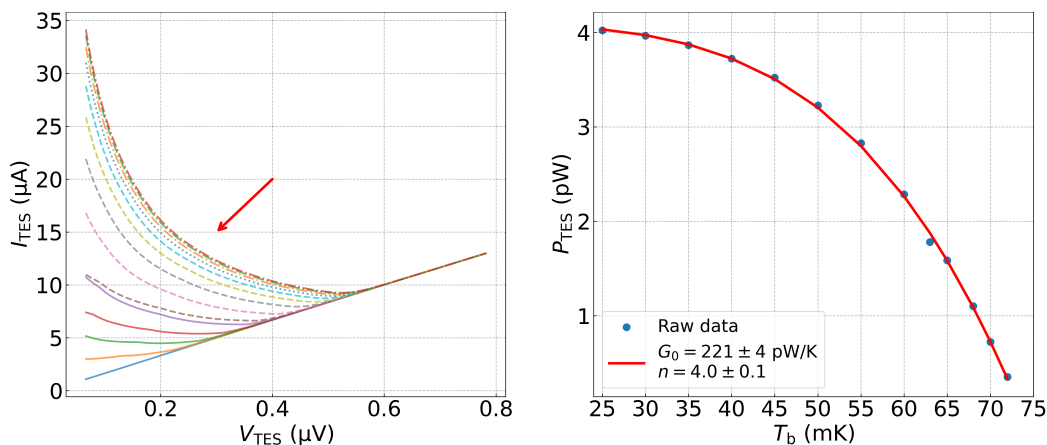


Figure 2: Electrical and thermal properties of the tested TES. Left: Measured I - V curves. Along the direction of the (red) arrow, T_b increases from 25 mK to 75 mK. Right: Measured P - T curve. It is derived from the I - V curves, with the best-fit model (see the main text) shown in solid (red) line.

4.2. Optical Illumination Measurements

Because heat capacity is kept small for TES devices, they are easily saturated when illuminated by an X-ray source. To characterize the energy resolution, we used a pulsed laser system, following [10]. In this setup, each pulse (containing N 3 eV photons) is used to simulate an X-ray photon (of energy $3N$ eV), when the duration of the pulse is much shorter than the response time of the devices. A monochromatic light source of wavelength 405 nm is located outside the refrigerator, and is driven by a waveform generator, allowing the pulse duration and optical power to be adjustable. The light enters the refrigerator through an optical fiber, which terminates just in front of the device under test. To suppress thermal crosstalk caused by

photons hitting the SiN outside the TES, a 100 μm -thick mask with 80 μm -diameter apertures was positioned 0.3 mm above the device.

For a given bias point, the average profile of TES response to laser pulses is shown in Fig. 3 (left panel). We use a double exponential function with rising and decaying time constants to fit the profile, and the best-fit model is also shown in the figure. The decaying time constant decreases with the bias point of the device, ranging roughly from 20 to 30 μs , as shown in the right panel of the figure.

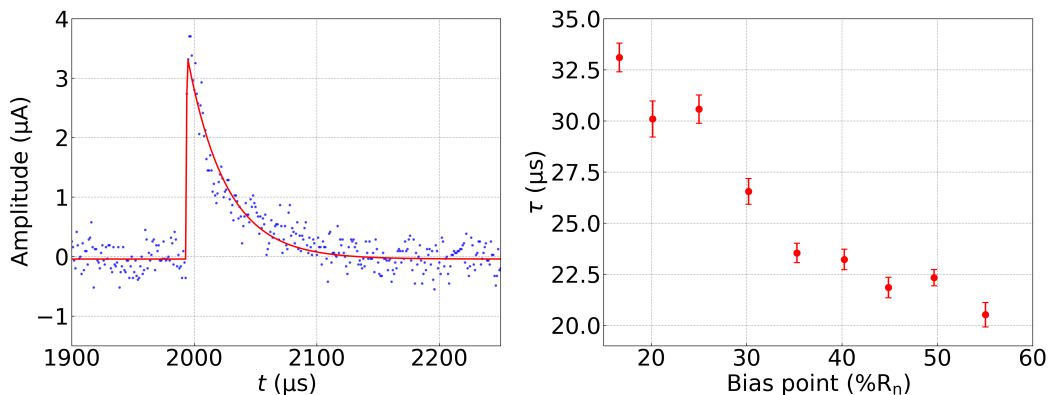


Figure 3: TES response to illuminating laser pulse. Left: Average pulse profile. The best-fit double-exponential function is shown in solid (red) line. Right: Pulse decaying time constant as a function of the TES bias point.

To determine the intrinsic energy resolution of the TES, we have lowered the intensity of the input laser light to enter single-photon mode. The pulse heights are measured using an optimal filter algorithm [11], and individual photon peaks are clearly identified in the pulse-height distribution, as shown in Fig. 4 (left panel). Here we note that these data were taken at a fixed laser power, and the mean photon number per pulse at this laser power was 1.98. Fitting the distribution with a series of Gaussian functions (with the centroids fixed at the respective photon energies) yields the resolution of the TES at different photon peaks. For the single-photon peak, the measured resolution is $\Delta E_1 = 1.1$ eV (FWHM). Taking the zero-photon peak as a noise contribution, we extract the intrinsic single-photon energy resolution of the device as $\Delta E = \sqrt{\Delta E_1^2 - \Delta E_0^2} = 0.46 \pm 0.09$ eV. Fig. 4 also shows the measured resolution for the first five photon peaks (in the right panel). The degradation in the resolution is apparent towards higher photon numbers.

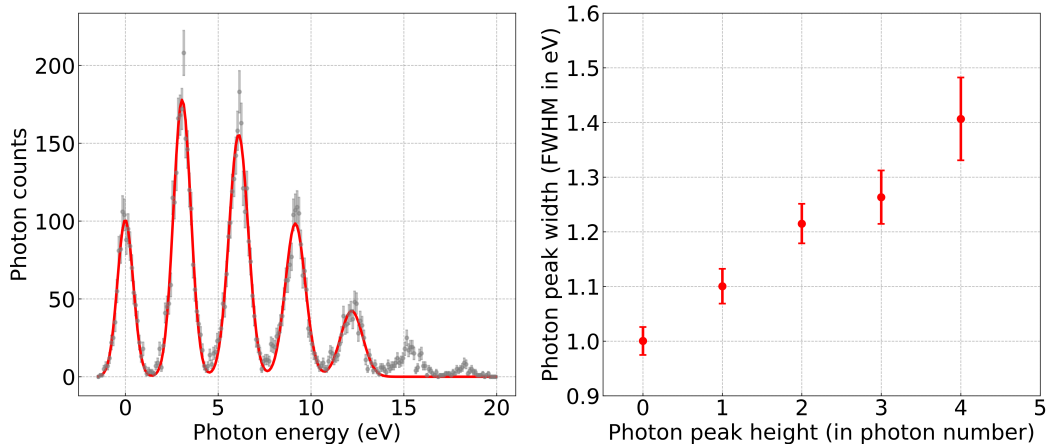


Figure 4: TES response to monochromatic light pulses, when biased at 25% R_n . Left: Pulse height distribution. The data are acquired at a constant laser power, and the mean photon number per pulse is determined to be 1.98. The pulse heights are calibrated, based on the separation of adjacent photon peaks (3 eV), and converted to photon energies. The best-fit model is shown in solid (red) line. Right: Energy resolution (FWHM). The results are shown for different photon peaks.

5. Microcalorimeter Characterization

We have selected two 10×10 microcalorimeter arrays for characterization, which adopt the same TES design as the one tested (see previous section), but are fabricated on a different batch of substrate wafers (see discussion below). The absorbers are made of pure gold and have an area of $240 \mu\text{m} \times 240 \mu\text{m}$.

5.1. Sample Devices

We have picked five devices for measurements, Devices S3-4 and S4-4 from one array (chip D3) and the remaining three devices from the other (chip D2). Four of the devices are tested with a ^{55}Fe source, as indicated in Tab. 1, and two are characterized electrically when shielded from the source (“Dark Test”). The measurements are affected by different SQUIDs used in the readout electronics. For SQUIDs with a coupling ratio ($\frac{1/M_{\text{fb}}}{1/M_{\text{in}}}$, where M_{fb} and M_{in} are mutual inductances with feedback coil and input coil, respectively) close to 12, we are not able to maintain stable operation at low bias points (below 20% R_n), so the corresponding results are missing.

Table 1: Information of measured microcalorimeters and corresponding SQUID coupling coefficients.

Chip	μ Cal pixel	TES size (μm^2)	^{55}Fe test	Dark test	$\frac{1/M_{\text{fb}}}{1/M_{\text{in}}}$
D3	S3-4	20×60	No	Yes	2.85
D3	S4-4	20×60	Yes	Yes	2.85
D2	S2-5	20×50	Yes	No	2.87
D2	S3-5	20×50	Yes	No	12.1
D2	S4-5	20×50	Yes	No	12.7

5.2. *I-V Measurements*

I-V characterization is carried out on each of the selected microcalorimeters for different base temperatures, and thermal conductance is then characterized through *P-T* curves. Tab. 2 summarizes the results. It is surprising that the thermal conductance is generally quite low, compared with the TES device (see Sec. 4.1), even without Si back-etching. The origin of such an abnormality is under investigation.

Table 2: Summary of *I-V* measurements of microcalorimeters.

Chip	μ Cal pixel	T_c (mK)	R_n (m Ω)	G (pW/K)	n
D3	S3-4	87	103	3.4	4.5
D3	S4-4	87	105	3.7	4.6
D2	S2-5	83	79	2.9	4.6
D2	S3-5	84	89	3.7	4.7
D2	S4-5	83	72	5.9	4.5

5.3. *X-ray Illumination Measurements*

The ^{55}Fe source is placed about 9 mm from a microcalorimeter array under test. No pinhole was used, so all pixels in the array are irradiated at the same time. For absorbers of area $240 \mu\text{m} \times 240 \mu\text{m}$, the expected event rate is approximately 1.2 counts/s/pixel.

Fig. 5 shows the average profile of X-ray pulses (in the left panel). We fit the profile with a double-exponential function to derive rising and decaying time constants, and show the best-fit model in the figure. The right panel of Fig. 5 shows the best-fit decaying time constant as a function of the bias

point for all devices tested. A minimum is observed at a bias of approximately 10% R_n .

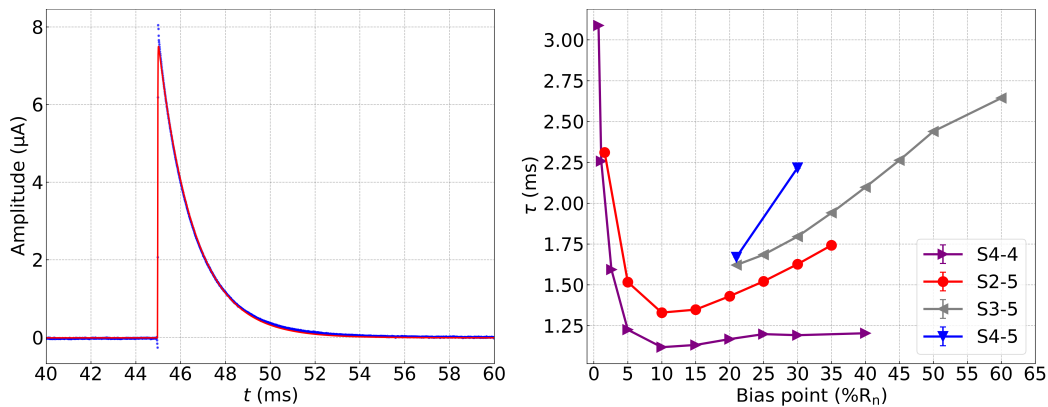


Figure 5: Results from ^{55}Fe illumination. Left: Average X-ray pulse profile. The best-fit double-exponential function is shown in solid (red) line. Right: Pulse decaying time as a function of bias. The results for all devices are shown. Note that no results at low bias points are shown for two of the devices due to issues with the SQUIDs used in the readout electronics (see the main text).

Again, pulse amplitudes are obtained with optimal filtering and are calibrated with the known energies of the Mn K_α and K_β lines. Fig. 6 shows the calibrated X-ray spectrum around the K_α line. The expected doublet is clearly resolved into $K_{\alpha 1}$ and $K_{\alpha 2}$. The energy resolution of a device is derived from simultaneously fitting all the lines (including K_β) with a series of Lorentzian functions (representing the natural profiles of the lines [12]) that are convolved with a Gaussian function (representing instrumental broadening). Among the devices tested, Device S2-5 shows the best resolution, 3.8 ± 0.2 eV (FWHM) at 5.9 keV, as shown in Fig. 6, when it is biased at $\sim 1.5\%$ R_n and operated at a base temperature of 20 mK.

We also measured the energy resolution of each device at the base temperature of 35 mK, and the results are shown in Fig. 7. All of our devices exhibit degradation in energy resolution towards high bias, with no apparent turning point at low bias, suggesting the absence of the so-called “excess noise” (e.g., [13], [14]). We note that no measurement with the pulsed laser system is attempted on these devices because they can not resolve 3 eV photons.

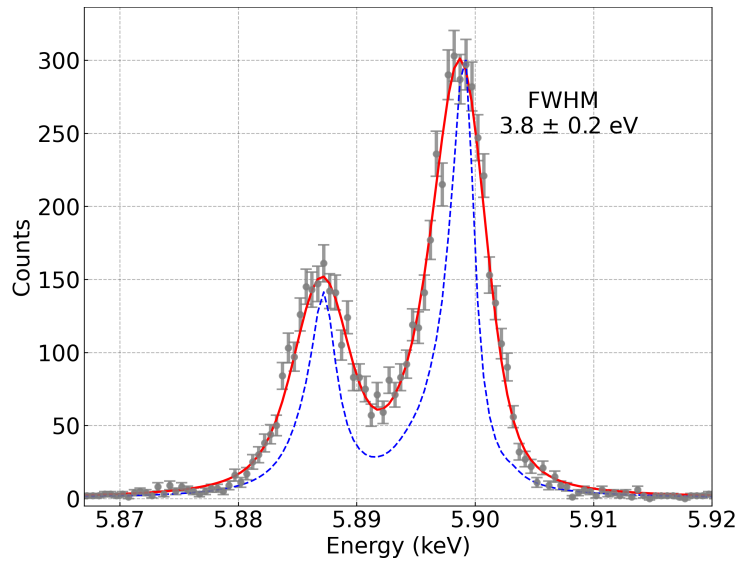


Figure 6: The measured X-ray spectrum of Device S2-5 around the Mn K_{α} line. The doublet is clearly resolved. The best-fit model is shown in solid (red) line, with the natural line profiles shown in dashed (blue) line.

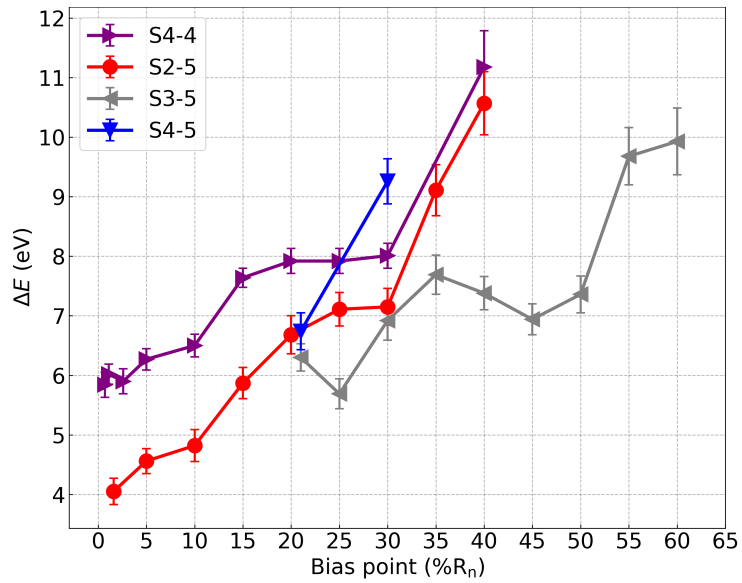


Figure 7: The measured energy resolution of the microcalorimeters at different biases.

5.4. Noise Spectrum Measurement

Fig. 8 shows the current noise spectra of Devices S4-4 and S2-5 that are obtained under illumination by the ^{55}Fe source, when biased at 5% R_n and operated at 35 mK. Each noise spectrum is computed using data in the segments of the time series that contain no apparent pulses. Also shown are the noise spectra of Devices S4-4 and S3-4 that are kept in the dark, when biased at the same level and operated at the same temperature for direct comparison. Note that the dark noise is higher for Device S4-4; this is due to a known issue with RF shielding, which is corrected for Device S3-4.

It is evident that the noise is significantly higher for the illuminated devices than for the shielded devices, at frequencies up to roughly 1 kHz, which corresponds to the thermal response bandwidth of the devices. This difference is very likely due to thermal crosstalk. When a neighboring pixel absorbs an X-ray photon, the heat generated propagates through the substrate to the pixel under test, thus introducing additional thermal fluctuation noise. The fundamental limit on the energy resolution of a microcalorimeter is set by the noise equivalent power (NEP) [5]:

$$\Delta E_{\text{FWHM}} = 2\sqrt{2\ln 2} \left(\int_0^\infty \frac{4}{|\text{NEP}(f)|^2} df \right)^{-1/2}. \quad (4)$$

The thermal crosstalk raises the NEP level of an illuminated device, degrading its energy resolution.

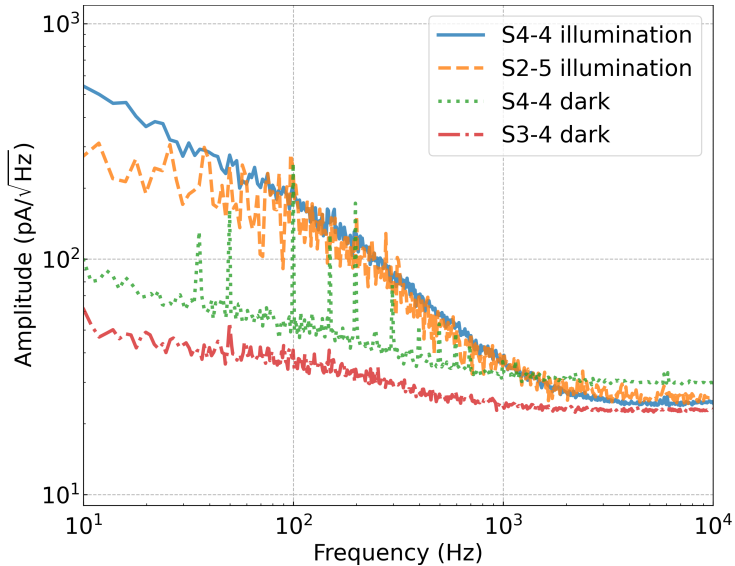


Figure 8: Current noise spectra of the microcalorimeters. The results are shown both for the illuminated devices and those in dark for direct comparison.

5.5. Complex Impedance Measurements

Complex impedance analysis is a useful tool for deriving the electro-thermal properties of a microcalorimeter [15], which are otherwise difficult to obtain. The measurements are made by adding a small sinusoidal perturbation to the bias voltage of a device over a selected range of frequencies (e.g., from 10 Hz to 10 kHz) and recording its current response. We fit the complex impedance data of the microcalorimeters using an intermediate-hanging (IH) model [15], as illustrated in Fig. 9. The model contains three heat capacities, with C_1 representing the absorber, C_{TES} the TES and C_2 the membrane between the TES and substrate. The thermal conductance between C_2 to the TES ($g_{\text{TES},2}$) is expected to be significantly larger than that between C_2 to the substrate ($g_{2,b}$).

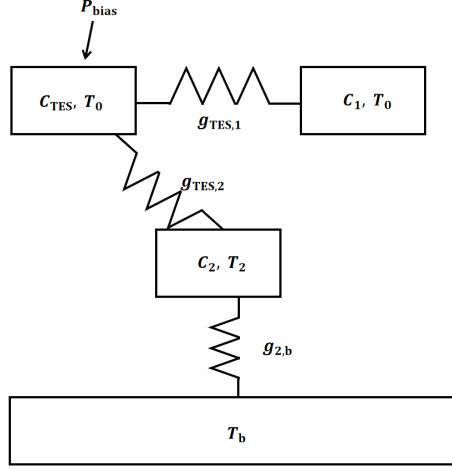


Figure 9: Three-block intermediate-hanging device model.

We adopt a differential evolution approach [16], to perform a simultaneous fitting of complex impedance and noise spectra. The data acquired at bias points of 5%, 10%, and 15% R_n are jointly fitted with the model, under the assumption that the parameters C_1 , C_2 , $g_{\text{TES},1}$, $g_{\text{TES},2}$ and T_2 are independent of the device bias, while α_i , β_i and $C_{\text{TES},i}$ are (with the subscript i denoting the i -th bias point). The conductance g_{eff} obtained from an I - V curve corresponds to the effective conductance of $g_{\text{TES},2}$ and $g_{2,b}$ that are connected in series, allowing $g_{2,b}$ to be derived. The values of R_{TES} , T_{TES} , and P are taken directly from the I - V measurements. In total, therefore, the model contains 14 free parameters. By constraining the bias-independent parameters across multiple bias points, the simultaneous fitting strategy narrows their allowed range of variation and yields more reliable and accurate results. In the mid-frequency range, the complex impedance fit is not fully satisfactory, suggesting that a higher-order model may be needed for a perfect description. To avoid overfitting, however, we do not pursue this further here. Once the common parameters are determined, α and β for the remaining bias points are obtained by fitting the complex impedance alone, as the thermal fluctuation noise (TFN) at these bias points is no longer significant compared with the readout noise.

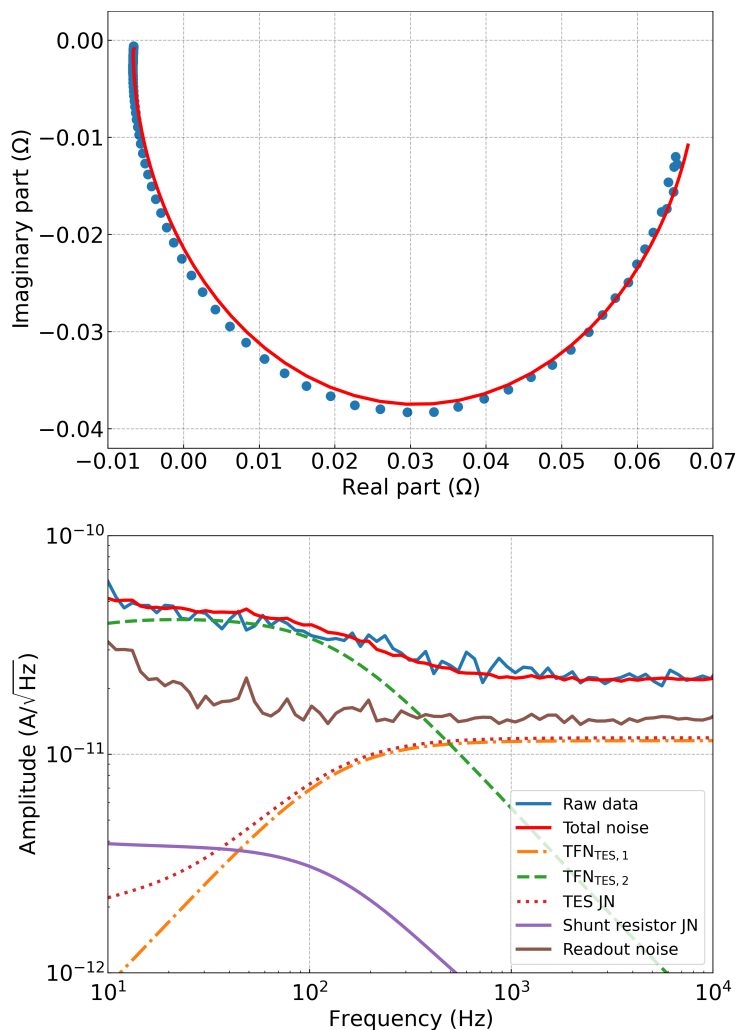


Figure 10: The complex impedance (top) and current noise spectrum (bottom) of Device S3-4 measured at the bias of $5\% R_n$. The best-fit model is shown in solid (red) line. The decomposition of the noise spectrum is shown in the bottom panel with each contribution indicated. Note that the heat exchange between the substrate and C_2 ($\text{TFN}_{b,2}$) stays below $10^{-12} \text{ A}/\sqrt{\text{Hz}}$ and is not displayed.

Fig. 10 shows the measured complex impedance and noise spectrum of Device S3-4, as an example, when it is biased at $5\% R_n$. The results of simultaneously fitting the two sets of data with the model are also shown in the figure. The best-fit values of the bias-independent common parameters are listed in Tab. 3. During the fitting, we found that C_{TES} is almost

unconstrained by the model, and its values are therefore not listed here. The fitting results for α and β are shown in Fig. 11.

The results suggest that the thermal fluctuation noise associated with heat exchange between the TES and C_2 ($\text{TFN}_{\text{TES},2}$) dominates at low frequencies, while the thermal fluctuation noise associated with heat exchange between the TES and C_1 ($\text{TFN}_{\text{TES},1}$) and the the Johnson noise (JN) of the TES together account for the high-frequency noise (after considering the readout noise). Again, there is no evidence for contribution from the “excess noise” here.

Table 3: Value of common parameters in complex impedance fitting.

C_1 (fJ/K)	C_2 (fJ/K)	T_2 (mK)	$g_{\text{TES},1}$ (nW/K)	$g_{\text{TES},2}$ (pW/K)
619 ± 5	134 ± 5	35.8 ± 0.3	136 ± 9	81 ± 4

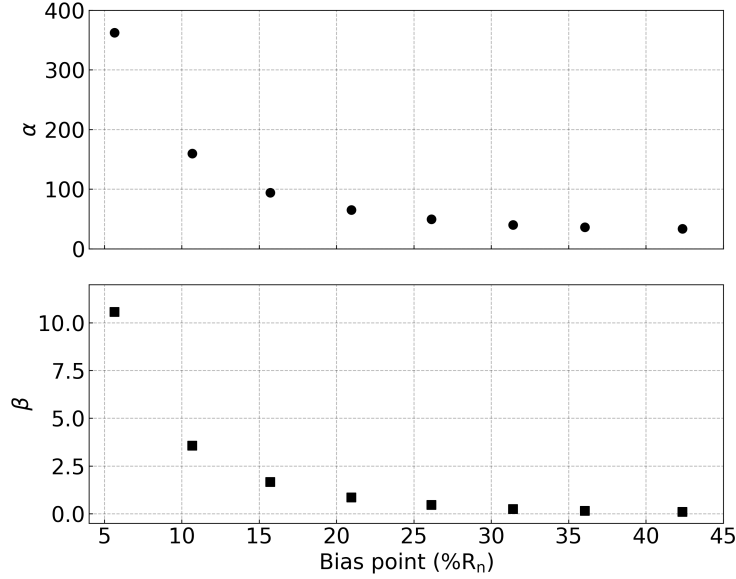


Figure 11: The temperature sensitivity α and current sensitivity β . Both were fitted from the complex impedance data at different bias points.

6. Discussion

6.1. Low Thermal Conductance of Microcalorimeters

We note that the measured thermal conductance G of the absorber-coupled TES (μCal) is markedly lower than that of the bare TES device. From the P - T fitting to the TES I - V curves, the extracted thermal exponent $n \approx 4$ suggests that the thermal transport may be dominated by Kapitza boundary resistance [17]. The Kapitza constant ($K_{\text{Kap}} = G/(4AT^3)$, where A is the area of the Kapitza interface, i.e., TES area) for bare TES and absorber-coupled TES (Device S2-5) is 14.5 and 1.3 $\text{W}/\text{K}^4/\text{m}^2$, respectively. This substantial discrepancy suggests that an additional large thermal resistance is present in the absorber-coupled devices, likely originating from one of the material interfaces introduced during micro-fabrication, possibly at the boundaries between the TES, SiN, SiO, and the Si substrate. We note that K_{Kap} in this work is significantly lower than other reported values, e.g., 125 $\text{W}/\text{K}^4/\text{m}^2$ [18]. The complex impedance fitting results in Sec. 5.5 further support this picture. Here $g_{\text{TES},2}$ is found to be large whereas $g_{2,b}$ is significantly smaller, indicating that the extra thermal resistance lies predominantly between the intermediate heat capacity C_2 and the heat bath, i.e., in the SiN/SiO/Si stack. We have examined the elemental composition of each layer with energy-dispersive X-ray spectroscopy (EDS), and found that the nitrogen content in the SiN layer is substantially lower than expected. Further investigation is under way to assess the origin of the extra thermal resistance.

6.2. Thermal Crosstalk in Illumination Test

In the pulsed-laser illumination experiment, a mask with a small pinhole is used to align the laser spot onto the TES, to prevent the photons from hitting the SiN membrane surrounding the TES, which causes significant thermal crosstalk, as shown in Fig. 12. In the figure, the widths of single-photon peaks are compared between two sets of measurements, the red dots correspond to a device (denoted TES1) for which the ratio of the pinhole area to the TES area is 3.14, whereas the blue triangles represent the device already shown in Fig. 4 (denoted TES2), for which the area ratio is 0.5 (and the pinhole diameter equals the short side of the TES). As the laser power is adjusted (quantified by the mean photon number per pulse), the energy resolution of TES1 degrades significantly toward high laser power, while that of TES2 remains roughly constant. We attribute the degradation

in energy resolution to the thermal crosstalk caused by photons depositing energy in the SiN membrane. On the other hand, Fig. 4 shows that, at a fixed laser power, the energy resolution deteriorates significantly as the photon number increases even with a small pinhole (c.f., [19]). This is probably not related to thermal crosstalk, but its origin is not clear.

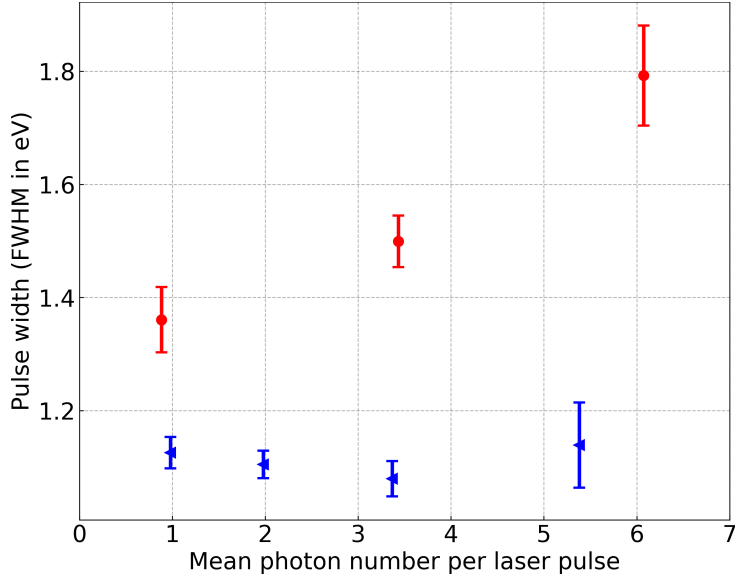


Figure 12: Effects for thermal crosstalk in optical illumination experiments. The measured widths of single-photon peaks are shown, as a function of laser power, for two setups: one with a pinhole of 3.14 times the TES area (in red dots) and the other with a collimating pinhole of 0.52 times the TES area (in blue triangles). See the main text.

In X-ray illumination of microcalorimeters, thermal crosstalk may also occur. In this case, the SiN membrane is almost entirely covered by the absorber, so the membrane-related thermal crosstalk is likely negligible. Unlike the optical illumination experiment, however, X-ray photons irradiate all pixels, so thermal crosstalk due to neighboring pixels could be significant. Such effects manifest themselves in the elevated noise levels of the pixels that are illuminated by X-rays (as shown in Fig. 8). To quantify the effects on the energy resolution, we convert the current noise $S_I(\omega)$ to the noise-equivalent power NEP² [7]:

$$\text{NEP}^2 = S_I(\omega)/s_I(\omega), \quad (5)$$

where $s_I(\omega) = -[1/(Z_{\text{circ}}I_0)] \cdot [(Z_{\text{TES}} - R_0(1+\beta))/(R_0(2+\beta))]$, $Z_{\text{circ}} = Z_{\text{TES}} + R_L + i\omega L$. Applying it to the noise spectrum of Device S3-4 (shielded from

X-ray illumination; see Tab. 1), from Eq. 4, we obtain a calculated energy resolution of 1.6 eV, at a bias point of 5% R_n , in the absence of illumination. Similarly, for Device S2-5 (under X-ray illumination), we get a calculated energy resolution of 3.6 eV, in the presence of illumination. Assuming that the devices are intrinsically similar, we estimate that the degradation in energy resolution observed under illumination reaches approximately 3.2 eV, which is most likely caused by thermal crosstalk.

A more accurate quantification of the effects of thermal crosstalk can be achieved by simultaneously reading out two adjacent pixels. Such measurements will be pursued in future work. To alleviate the effects, we plan to improve the thermal conductance between the TES and the heat sink, following [20].

7. Conclusion

We have fabricated TES and microcalorimeter arrays, based on Mo/Cu bilayer films, and measured their electrothermal properties. The results confirm that the designed TES contributes little to the energy resolution of the TES microcalorimeter. At the energies of Mn K_α lines (~ 5.9 keV), the best energy resolution obtained is 3.8 ± 0.2 eV among the tested microcalorimeters. Comparing the noise spectra of the illuminated and shield devices, we have identified pixel-to-pixel thermal crosstalk as a significant factor that degrades the energy resolution in our experimental setup. This is an area for improvement in the future.

We will continue to investigate the origin of the abnormally low thermal conductance of the tested TES microcalorimeters by comparing the properties of different batches of arrays that have already been fabricated, including those with substrate Si fully etched from the back. The development is also underway to replace small-area pure Au absorbers with large-area Au/Bi ones, which are baselined for HUBS. It would, in principle, maintain a similar energy resolution since the heat capacity is designed to be the same. However, the reduction of Au thickness will probably cause a degradation of energy resolution due to the position dependence effect on the pulse [21], which needs further investigation. Finally, efforts will be made to improve the uniformity of pixels within an array, between arrays in the same batch, and between different batches.

Acknowledgement

We wish to thank Dr. Jingjing Li and her team at the National Institute of Metrology for providing the input SQUIDs used in our experiment. Sifan Wang wishes to acknowledge support from the China Postdoctoral Science Foundation through Grant GZB20240377. This work was supported in part by the National Natural Science Foundation of China through Grant 12220101004, by the Ministry of Science and Technology of China through Grant 2022YFC2205100, and by the China National Space Administration through a technology development grant.

References

- [1] M. Fukugita, C. Hogan, P. Peebles, The cosmic baryon budget, *The Astrophysical Journal* 503 (2) (1998) 518.
- [2] W. Cui, L.-B. Chen, B. Gao, F.-L. Guo, H. Jin, G.-L. Wang, L. Wang, J.-J. Wang, W. Wang, Z.-S. Wang, et al., Hubs: hot universe baryon surveyor, *Journal of Low Temperature Physics* 199 (1) (2020) 502–509.
- [3] W. Cui, J. Bregman, M. Bruijn, L.-B. Chen, Y. Chen, C. Cui, T.-T. Fang, B. Gao, H. Gao, J.-R. Gao, et al., Hubs: a dedicated hot circumgalactic medium explorer, in: *Space Telescopes and Instrumentation 2020: Ultraviolet to Gamma Ray*, Vol. 11444, SPIE, 2020, pp. 470–481.
- [4] D. McCammon, S. Moseley, J. Mather, R. Mushotzky, Experimental tests of a single-photon calorimeter for x-ray spectroscopy, *Journal of applied physics* 56 (5) (1984) 1263–1266.
- [5] D. McCammon, Thermal equilibrium calorimeters—an introduction, in: *Cryogenic particle detection*, Springer, 2005, pp. 1–34.
- [6] S. Wang, G. Wang, N. Chen, Y. Chen, W. Cui, J. Ding, F. Li, Y. Liang, Q. Wang, Y. Wang, Development of superconducting microcalorimeters for the hubs mission, *Superconductivity* 4 (2022) 100027.
- [7] K. D. Irwin, G. C. Hilton, Transition-edge sensors, in: *Cryogenic particle detection*, Springer, 2005, pp. 63–150.

- [8] Y. Wang, S. Wang, J. Ding, Y. Chen, W. Cui, R. Huang, C. Li, F. Li, Y. Liang, H. Jin, et al., Study of long-term stability of mo-cu bilayer films, *Superconductor Science and Technology* 35 (9) (2022) 095005.
- [9] J. Clarke, A. I. Braginski, *The SQUID handbook: Applications of SQUIDS and SQUID systems*, John Wiley & Sons, 2006.
- [10] F. Jaeckel, C. Ambarish, N. Christensen, R. Gruenke, L. Hu, D. McCammon, M. McPheron, M. Meyer, K. Nelms, A. Roy, et al., Energy calibration of high-resolution x-ray tes microcalorimeters with 3 ev optical photons, *IEEE Transactions on Applied Superconductivity* 29 (5) (2019) 1–4.
- [11] A. Szymkowiak, R. Kelley, S. Moseley, C. Stahle, Signal processing for microcalorimeters, *Journal of Low Temperature Physics* 93 (3) (1993) 281–285.
- [12] G. Holzer, M. Fritsch, M. Deutsch, J. Hartwig, E. Forster, K a1, 2 and k b1, 3 x-ray emission lines of the 3d transition metals, *Physical Review-Section A-Atomic Molecular and Optical Physics* 56 (6) (1997) 4554–4568.
- [13] G. Fraser, On the nature of the superconducting-to-normal transition in transition edge sensors, *Nuclear Instruments and Methods in Physics Research Section A: Accelerators, Spectrometers, Detectors and Associated Equipment* 523 (1-2) (2004) 234–245.
- [14] D. Brandt, G. W. Fraser, Analytical expressions for transition edge sensor excess noise models, *Nuclear Instruments and Methods in Physics Research Section A: Accelerators, Spectrometers, Detectors and Associated Equipment* 620 (2-3) (2010) 294–298.
- [15] I. J. Maasilta, Complex impedance, responsivity and noise of transition-edge sensors: Analytical solutions for two-and three-block thermal models, *Aip Advances* 2 (4) (2012).
- [16] A. P. Helenius, T. Puurtinen, K. Kinnunen, I. Maasilta, Simultaneous noise and impedance fitting to transition-edge sensor data using differential evolution, *Journal of Low Temperature Physics* 200 (5) (2020) 213–219.

- [17] E. T. Swartz, R. O. Pohl, Thermal boundary resistance, *Reviews of modern physics* 61 (3) (1989) 605.
- [18] H. Hoever, Thermal physics of transition edge sensor arrays, *Nuclear Instruments and Methods in Physics Research Section A: Accelerators, Spectrometers, Detectors and Associated Equipment* 559 (2) (2006) 702–705, proceedings of the 11th International Workshop on Low Temperature Detectors.
- [19] F. T. Jaeckel, C. Ambarish, H. Dai, S. Liu, D. McCammon, M. McPheron, K. L. Nelms, A. Roy, H. R. Stueber, S. R. Bandler, et al., Calibration and testing of small high-resolution transition edge sensor microcalorimeters with optical photons, *IEEE Transactions on Applied Superconductivity* 31 (5) (2021) 1–5.
- [20] F. Finkbeiner, C. Bailey, S. Bandler, R. Brekosky, A. Brown, J. Chervenak, M. Eckart, R. Kelley, D. Kelly, C. Kilbourne, et al., Development of embedded heatsinking layers for compact arrays of x-ray tes microcalorimeters, *IEEE transactions on applied superconductivity* 21 (3) (2010) 223–226.
- [21] S. Wang, M. Bruijn, L. Gottardi, K. Nagayoshi, M. Ridder, M. de Wit, J.-R. Gao, W. Cui, Modeling the effects of position dependence in large-absorber x-ray tes microcalorimeters, *Journal of Applied Physics* 138 (3) (2025).